IEEE Photonics Journal
An IEEE Photonics Society Publication

Open Access

Spectroscopic Properties and Continuous Wave Laser Performances at 1064 nm of Nd^{3+}: LuAG Transparent Ceramic

Volume 9, Number 2, April 2017

Chaoyang Ma
Jiangfeng Zhu
Zhongqi Hu
Zicheng Wen
Jiaqi Long
Xuanyi Yuan
Yongge Cao

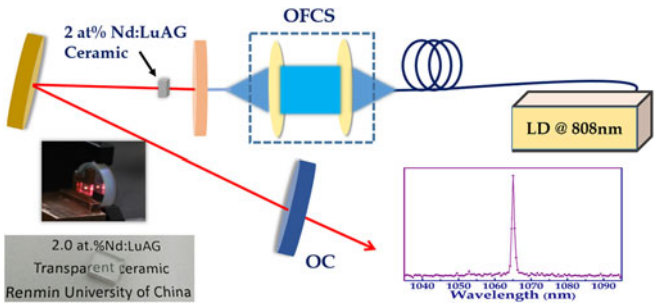

DOI: 10.1109/JPHOT.2017.2682850
1943-0655

IEEE photonics SOCIETY

IEEE

Spectroscopic Properties and Continuous Wave Laser Performances at 1064 nm of Nd^{3+}: LuAG Transparent Ceramic

Chaoyang Ma,[1] Jiangfeng Zhu,[2] Zhongqi Hu,[2] Zicheng Wen,[1] Jiaqi Long,[1] Xuanyi Yuan,[1] and Yongge Cao

[1]Key Laboratory of Opto-Eletronic Functional Materials and Micro-Nano Devices, Department of Physics, School of Science, Renmin University of China, Beijing 100872, China
[2]School of Physics and Optoelectronic Engineering, Xidian University, Xi'an 710071, China

DOI:10.1109/JPHOT.2017.2682850

Manuscript received January 1, 2017; revised March 7, 2017; accepted March 13, 2017. Date of publication March 15, 2017; date of current version April 5, 2017. This work was supported in part by the Programs of National Natural Science Foundation of China under Grant 51272282 and Grant 51302311 and in part by the Significant Achievement Transformation Project of Colleges and Universities of the Central in Beijing (ZD20141000201), supported by Beijing Municipal Education Commission.
Corresponding author: Y. Cao (e-mail: caoyongge@ruc.edu.cn).

Abstract: A transparent 2 at% Nd^{3+}-doped $Lu_3Al_5O_{12}$ (LuAG) ceramic was fabricated by using tape-casting method and solid-state sintering technology. Based on the room temperature absorption spectrum, the three J–O intensity parameters were calculated with Judd–Ofelt analysis, and then, the radiative transition rates and branching ratios of transitions from $^4\mathbf{F}_{3/2}$ manifold to the $^4\mathbf{I}_{J'}$ ($\mathbf{J'} = 13/2, 11/2, 9/2$) lower lying multiple manifolds were determined. The quantum efficiency of 80.4% was evaluated from the measured fluorescence lifetime and the radiative lifetime of the $^4\mathbf{F}_{3/2}$ manifold state. Also, the inter-Stark energy levels of the $4\mathbf{I}_{J'}$ manifolds were performed, and the peak emission cross sections of the $^4\mathbf{F}_{3/2} \rightarrow {}^4\mathrm{I}_{J'}$ intermanifold transitions were determined. The total emission cross section for $^4\mathbf{F}_{3/2} \rightarrow {}^4\mathbf{I}_{9/2}$, $^4\mathbf{I}_{11/2}$, and $^4\mathbf{I}_{13/2}$ transitions was calculated to be 7.41×10^{-20} cm^2, 29.83×10^{-20} cm^2, and 10.53×10^{-20} cm^2, respectively. Finally, under an 808 nm diode laser pumping, the continuous wave laser performances of the Nd:LuAG transparent ceramic were investigated.

Index Terms: Diode-pumped lasers, oxide materials, optical and other properties, solid-state lasers, spectroscopy.

1. Introduction

Nd^{3+} is one of the most widely investigated lanthanide ions in glasses, crystals, and ceramics host due to its important transition of $^4F_{3/2} \rightarrow {}^4I_{11/2}$. As a promising candidate for high power laser materials, Nd^{3+}-doped $Y_3Al_5O_{12}$ (Nd:YAG) ceramic has attracted much attention because of its remarkable advantages such as excellent spectral characteristic, structural stability and high thermal conductivity [1]–[5]. $Lu_3Al_5O_{12}$ (LuAG), the same as YAG, belongs to the garnet family. Nd:LuAG owns the advantages of high thermal conductivity (9.6 W/m·K [6]), a relatively long fluorescence lifetime (277 μs [7]), and, especially, the moderate emission cross-section (9.67×10^{-20} cm^2 [8]), as well as outstanding physical and chemical properties, making it a very promising laser gain medium. In comparison with classical Nd:YAG laser materials, Nd:LuAG materials have

two advantages. The first one is that Nd:LuAG owns smaller splitting of $^4F_{3/2}$ sate ($67\,cm^{-1}$) than that of Nd:YAG ($84\,cm^{-1}$) [9], and this generates a higher amplification at 1064 nm lasing wavelength. Second, atomic mass difference between Y^{3+} (88.9 g/mol) and Nd^{3+} (144 g/mol) is much bigger than that between Lu^{3+} (175 g/mol) and Y^{3+} ions, and, as a result, Nd:LuAG exhibits superior thermal conductivity in the case of high rare-earth doping concentrations or operating at high temperature [10]. The first Nd:LuAG crystal was reported in 2009 [7], and the laser operation at 1064 nm was demonstrated. The first fabricated Nd:LuAG transparent ceramic was reported in 2012 [11]. Nowadays, Nd:LuAG ceramics attract much more attention to obtain highly optical quality and optimized performance [12]–[17]. Besides, 2.5 at% Yb:LuAG [18] and 0.8 at% Ho:LuAG [19] laser ceramics were reported with CW laser output. Recently, our group also fabricated the Yb^{3+}- or Nd^{3+}-doped LuAG transparent ceramics [20]–[22].

In this paper, we report the fabrication of 2at% Nd:LuAG transparent ceramics by using tape-casting method and solid-state reactive sintering in vacuum. The Judd-Ofelt (J-O) [23], [24] analysis of Nd^{3+} ions are performed. The three J-O intensity parameters Ω_t (t = 2, 4, 6) are determined from absorption spectrum and refractive index of the ceramic sample. A series of other optical properties, such as absorption line strength, radiative transition probabilities, fluorescence branch ratios, and radiative lifetime are systematically evaluated from these parameters. The internal quantum efficiency is calculated from the ratio of the fluorescence lifetime to the radiative lifetime. Besides, the inter-Stark energy levels of the $^4I_{J'}$ ($J' = 13/2, 11/2, 9/2$) manifolds are performed and the peak emission cross sections of the $^4F_{3/2} \rightarrow {}^4I_{J'}$ ($J' = 13/2, 11/2, 9/2$) inter-manifold transitions were determined. Finally, CW laser performances of the Nd:LuAG transparent ceramic are investigated under an 808 nm diode laser pumping.

2. Experimental Details

2.1 Preparation of Nd:LuAG Ceramic

The entire fabricating procedure is similar to that of the previous report [22]. Commercially available α-Al_2O_3 powder (Sumitomo Chemical Co. Ltd, purity > 99.99%), Lu_2O_3 powder (Jiangyin Jiahua Advanced Material Resources Co. Ltd., purity > 99.99%), and Nd_2O_3 powder (Alfa Aesar, purity > 99.99%) were used as the raw materials without further purifying. The powders were weighted precisely according to the stoichiometry of $(Nd_{0.02}Lu_{0.98})_3Al_5O_{12}$ and mixed with the solvent of 40 wt% ethanol and 60 wt% xylene. The mixed slurry with a solid content of 65% was then ball-milled using a planetary ball mill for 24 h. Subsequently, the selected binder and plasticizer were added into the obtained slurry and then milled for another 24 h. After that, the tape casting process was conducted and the height between the blade and the substrate was 600 μm with a casting speed of 0.5 m/min, and tapes with thickness of 0.15 mm were dried at room temperature and then cut into slices. The appropriate number of layers of the slices were stacked and laminated at 120 °C under 20 Mpa for 10 min to obtain the green bodies. The added organics were burned out in oxygen atmosphere at 800 °C for 20 h, and then the burned green bodies were sintered at 1850 °C for 15 h in a high-temperature vacuum sintering furnace with the vacuum level better than 10^{-3} Pa. the as-sintered ceramics were then annealed in the air at 1450 °C for 10 h to eliminate the oxygen vacancies and internal stress. Finally, the Nd:LuAG transparent ceramics were mirror-polished using different grades of SiC and Al_2O_3 slurries.

2.2 Characterization

The phase identification of the ceramics was carried out by X-ray diffraction (XRD), and the cross-section morphologies were characterized by a scanning electron microscopy (SEM, JSM-670, JEOL) equipped with the energy dispersive X-ray (EDX) spectrum. The in-line transmittance curves of the mirror-polished ceramics were measured with a UV/Vis/NIR spectrophotometer (Lambda-950, PerkinElmer). The indices of refraction of the Nd:LuAG ceramic for various wavelength were calculated using Sellmeier's dispersion equation, of which the coefficients were determined by fitting

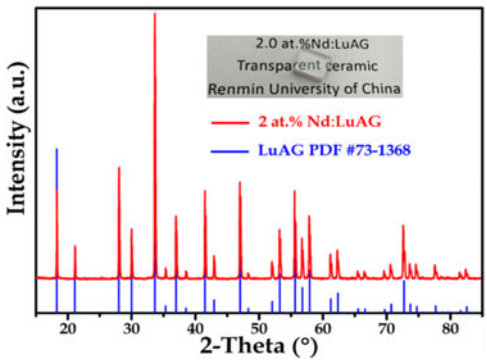

Fig. 1. XRD patterns of the 2 at% Nd:LuAG transparent ceramic. The bottom lines show the standard XRD pattern of pure $Lu_3Al_5O_{12}$ (PDF#73-1368). (Inset) Fabricated sample.

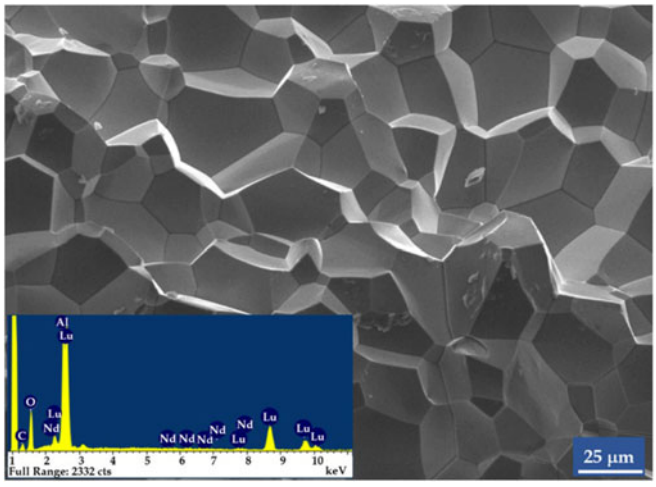

Fig. 2. Cross-section SEM morphologies of the prepared 2 at% Nd:LuAG transparent ceramic. (Inset) Corresponding EDS spectrum.

the five data measured with a ellipsometer (ES01, Ellitop Scientific Co., LTD). The fluorescence spectra, as well as decay curves at 1064 nm, were recorded using a NanoLog infrared fluorescence spectrophotometer (Nanolog FL3-2iHR, Horiba Jobin Yvon) by taking a Xenon lamp as the exciting source. Laser performances of Nd:LuAG transparent ceramic were studied with an 808 nm fiber-coupled diode laser system and will be discussed in detail later.

2.3 Phase and Morphologies

The X-ray diffraction (XRD) patterns of transparent $(Nd_{0.02}Lu_{0.98})_3Al_5O_{12}$ ceramic along with the standard patterns of pure $Lu_3Al_5O_{12}$ are shown in Fig. 1. All the diffraction peaks of Nd^{3+}-doped LuAG transparent ceramic can be well indexed to Ia-3d (230) space group of cubic $Lu_3Al_5O_{12}$ (PDF#73-1368). No traces of other phases or impurities were detected, which suggested that the doping of Nd^{3+} ions did not generate any impurity or induce significant changes in the host structure, and that the ceramic had been totally transformed into pure LuAG phase after sintering at 1850 °C for 15 h. Fig. 2 reports the SEM micrographs of the fracture surfaces of the fabricated Nd3+-doped LuAG transparent polycrystalline ceramic. There are almost no pores and secondary phases at the grain boundaries or inner grains. Meanwhile, the grain boundaries appear clean and fully dense, and the relative densities measured by the Archimedes method was 99.4%. The inserted EDS spectrum

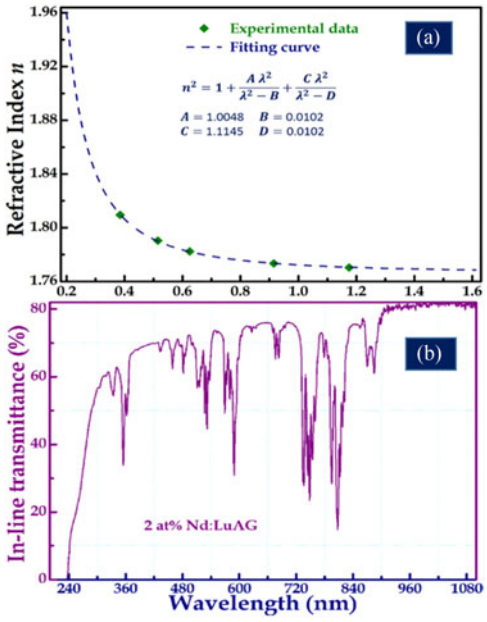

Fig. 3. (a) Changes of refractive indices of the 2 at% Nd:LuAG transparent ceramic. Fitting curve represents the fitted Sellmeier's equation to the experimental data. (Inset) Fitted Sellmeier's parameters. (b) In-line transmittance spectrum of 2 at% Nd:LuAG ceramic

confirmed Al, Lu, Nd, and O signals. Besides, the proportions of these atoms were calculated to be 1.95 at% Nd:$Lu_3Al_{4.8}O_{11.9}$, which was in close proximity to the theoretical percentages.

3. Results and Discussion

3.1 Judd-Ofelt (J-O) Analysis

The indices of refraction of the ceramic 2 at% Nd:LuAG were measured at five different wavelengths using a ellipsometer. The refractive indices for various wavelengths were calculated using Sellmeier's dispersion equation, which is expressed as follows [25]:

$$n^2(\lambda) = 1 + \frac{A\lambda^2}{\lambda^2 - B} + \frac{C\lambda^2}{\lambda^2 - D} \tag{1}$$

where λ is the wavelength in microns; and A, B, C, and D are Sellmeier's coefficients. Sellmeier's coefficients were determined by fitting the measured five data points to (1), as shown in Fig. 3. The Sellmeier's coefficients were calculated to be A = 1.0048, B = D = 0.0102, and C = 1.1145. Fig. 4 shows the wavelength dependent absorption coefficient ($\alpha(\lambda)$), which was calculated from the transmission spectrum at room temperature using the relation

$$T(\lambda) = (1 - R(\lambda))^2 \exp(-\alpha(\lambda)\, t) \tag{2}$$

where t is the thickness of the ceramic specimen, and T(λ) and R(λ) are the transmittance (see Fig. 3(b)) and reflectivity at the wavelength λ, respectively. According to Sellmeier's equation, the reflectivity could be calculated by the following formula:

$$R(\lambda) = (n(\lambda) - 1)^2 / (n(\lambda) + 1)^2. \tag{3}$$

The absorption spectrum of the ceramic consists of a large number of absorption bands ascribed to the transitions from the $^4I_{9/2}$ ground level within the 4f shell of Nd^{3+} ions.

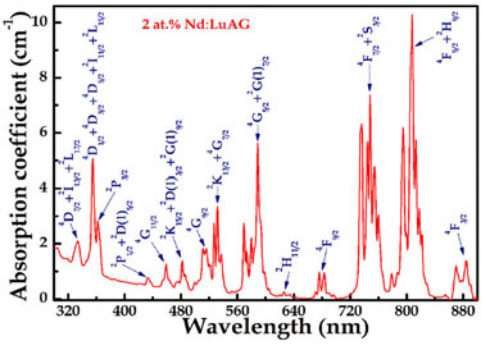

Fig. 4. Absorption spectrum of 2 at% Nd:LuAG transparent ceramic (all transitions from $^4I_{9/2}$) at room temperature.

Fourteen absorption bands and corresponding twenty-seven transitions are detected in the absorption spectrum, as shown in Fig. 4. These absorption bands are chosen to determine the phenomenological J-O parameters for ceramic Nd^{3+}-doped LuAG. The absorption line strengths, $S_{meas}(J \rightarrow J')$, of the transitions between the ground $^4I_{9/2}$ ($J = 9/2$) manifold and the excited J' manifolds are determined using the following equation [25]–[27]:

$$S_{meas}\left(J \rightarrow J'\right) = \frac{3h\varepsilon_0 c\left(2J+1\right) n\left(\bar{\lambda}\right)}{8\pi^3 \bar{\lambda} e^2 N_0}\left[\frac{9}{\left(n\left(\bar{\lambda}\right)^2+2\right)^2}\right]\int \alpha\left(\lambda\right) d\lambda \tag{4}$$

where h is the Planck Constant, ε_0 is the permittivity of vacuum, c is the speed of light in vacuum, e is the charge on one electron, N_0 is the concentration of Nd^{3+} ions doped into the LuAG host, $\bar{\lambda}$ is the mean wavelength of certain absorption band, $n(\bar{\lambda})$ is the refractive index of ceramic Nd:LuAG at mean wavelength $\bar{\lambda}$, $\alpha(\lambda)$ is the linear absorption coefficient at the wavelength λ, $\int \alpha(\lambda)d\lambda$ is the integrated absorption coefficient (i.e., area under the absorption band), $(2J+1)$ is the degeneracy of the ground state, and $[9/(n(\bar{\lambda})^2+2)^2]$ represents the Lorentz field correction for the Nd^{3+} ions in the dielectric host medium. The measured mean wavelength ($\bar{\lambda}$), refractive indices $n(\bar{\lambda})$, integrated absorption coefficients ($\int \alpha(\lambda)d\lambda$) are listed in Table 1. Combining with (4), the absorption line strengths ($S_{meas}(J \rightarrow J')$) were calculated for several Nd^{3+} ions transitions and tabulated in Table 1.

According to the Judd-Ofelt theory, the line strength is adopted to describe the electric-dipole transition between two of the eigenstates of the ions. The line strength $S_{calc}(J \rightarrow J')$ between initial J manifold and final J' manifold can be linearly expressed as [25]–[27]

$$S_{calc}\left(J \rightarrow J'\right) = \sum\nolimits_{t=2,4,6} \Omega_t \left|\varphi J U^{(t)} \varphi' J'\right|^2 \tag{5}$$

where Ω_t ($t = 2, 4, 6$) are the Judd-Ofelt phenomenological parameters and tend to vary from host to host with the local environment due to the charges and positions of the ligand ions.

$|\langle \varphi J \| U^{(t)} \| \varphi' J' \rangle|^2$ ($t = 2,\ 4,\ 6$) are the doubly reduced matrix elements of the unit tensor operators $U^{(t)}$ of rank t ($t = 2,\ 4,\ 6$) depend only on angular momentum while are independent of the host, and are taken from the literature [23]. For two or more manifolds, the reduced matrix elements are calculated to be the sum of the corresponding matrix elements, and the values of them for the fourteen absorption bands are given in Table 1. With the experimentally measured line strength $S_{meas}(J \rightarrow J')$, the J-O parameters can be calculated by means of the least-square method:

$$\delta\left(J \rightarrow J'\right) = \sum_{J'}\left[S_{meas}\left(J \rightarrow J'\right) - S_{calc}\left(J \rightarrow J'\right)\right]^2 \tag{6}$$

$$\partial\delta\left(J \rightarrow J'\right)/\partial\Omega_t = 0 \qquad (t = 2,\ 4,\ 6)\,. \tag{7}$$

TABLE 1
Values of Reduced Matrix Elements, Measured and Calculated Absorption Line Strengths for the Absorption Transitions of Nd^{3+} ($4f^3$) Doped LuAG Ceramic at 300 K

Transition (from $^4I_{9/2}$)	$[U^{(2)}]^2$	$[U^{(4)}]^2$	$[U^{(6)}]^2$	$\bar{\lambda}$ (nm)	$n(\bar{\lambda})$	$\int \alpha(\lambda)d\lambda$ (10^{-7})	S_{meas} (10^{-21} cm^2)	S_{calc} (10^{-21} cm^2)
$^4D_{7/2}+^2I_{13/2}+^2L_{17/2}$	0.0001	0.0060	0.0110	334	1.8253	5.46	0.2755	0.0620
$^4D_{1/2}+^4D_{3/2}+^4D_{5/2}+^2I_{11/2}+^2L_{15/2}$	0.0052	0.5529	0.0580	355	1.8180	21.36	1.0202	1.1399
$^2P_{3/2}$	0	0.0011	0.0007	362	1.8158	8.99	0.4217	0.0051
$^2P_{1/2}+^2D(1)_{5/2}$	0	0.0356	0.0022	433	1.8002	0.48	0.0191	0.0658
$^4G_{11/2}$	0	0.0054	0.0082	459	1.7963	2.36	0.0887	0.0476
$^2K_{15/2}+^2D(1)_{3/2}+^2G(1)_{9/2}$	0.0012	0.0433	0.0325	481	1.7935	4.78	0.1719	0.2235
$^4G_{9/2}$	0.0043	0.0570	0.0370	513	1.7901	17.13	0.5791	0.2683
$^2K_{13/2}+^4G_{7/2}$	0.0711	0.1814	0.0946	531	1.7884	23.07	0.7546	0.7798
$^4G_{5/2}+^2G(1)_{7/2}$	0.9735	0.5701	0.0592	589	1.7842	60.29	1.7849	1.7883
$^2H_{11/2}$	0.0001	0.0026	0.0104	626	1.7821	0.13	0.0036	0.0538
$^4F_{9/2}$	0.0007	0.0087	0.0446	683	1.7795	2.99	0.0766	0.2274
$^4F_{7/2}+^2S_{3/2}$	0.0011	0.0443	0.6621	747	1.7772	123.54	2.8975	3.2381
$^4F_{5/2}+^2H_{9/2}$	0.0106	0.2447	0.5118	807	1.7756	151.95	3.3033	2.8362
$^4F_{3/2}$	0	0.2282	0.0536	885	1.7740	21.71	0.4309	0.6111

$\Omega_2 = 0.63 \times 10^{-21}$ cm^2, $\Omega_4 = 1.55 \times 10^{-21}$ cm^2, $\Omega_6 = 4.78 \times 10^{-21}$ cm^2, rms deviation $= 0.25 \times 10^{-21}$ cm^2.

The calculated values of J-O parameters are $\Omega_2 = 0.63 \times 10^{-21}$ cm^2, $\Omega_4 = 1.55 \times 10^{-21}$ cm^2, and $\Omega_6 = 4.78 \times 10^{-21}$ cm^2. The spectroscopic quality factor, $X = \Omega_4/\Omega_6$, for the Nd:LuAG ceramic is calculated to be 0.32. However, the values of X has been found to vary from 0.2 to 1.5 in a wide range of Nd^{3+}-doped hosts [28]. In the case of $X \leq 1$, the efficiency of the $^4F_{3/2} \rightarrow {}^4I_{11/2}$ transition is enhanced, while the larger the value of X, the more intense the transition $^4F_{3/2} \rightarrow {}^4I_{9/2}$ is. These three J-O parameters are used to calculate the theoretical value of absorption line strength $S_{calc}(J \rightarrow J')$ from (5), as shown in Table 1. What's more, the accuracy of the least-square method is given by the rms deviation:

$$\Delta S_{rms} = \left[(q-p)^{-1} \sum (S_{meas} - S_{calc})^2\right]^{1/2} \tag{8}$$

$$S_{rms} = \left[q^{-1} \sum {S_{calc}}^2\right]^{1/2} \tag{9}$$

where q is the number of the absorption bands analyzed, and p is the number of the J-O parameters. Here, the values of p and q are 3 and 14, respectively. Therefore, the measured and calculated line strengths given in Table 1 provide an rms deviation of 0.25×10^{-21} cm^2. The rms line strength was determined to be 1.31×10^{-21} cm^2. The ratio of these two values yields an rms error of about 19%, which is the relative error of fit and falls at the lower end of the range of 5%–25%, as obtained by the application of the J-O theory to other laser materials [29], [30].

3.2 Branching Ratios and Fluorescence Decay

The J-O parameters can then to be applied to (5) to calculate the emission line strength corresponding to the transitions from the upper manifold ^4F_J ($J = 3/2$) to the corresponding lower lying multiple manifolds $^4I_{J'}(J' = 13/2, 11/2, 9/2)$ of Nd^{3+} in LuAG ceramic, as shown in Fig. 5. The

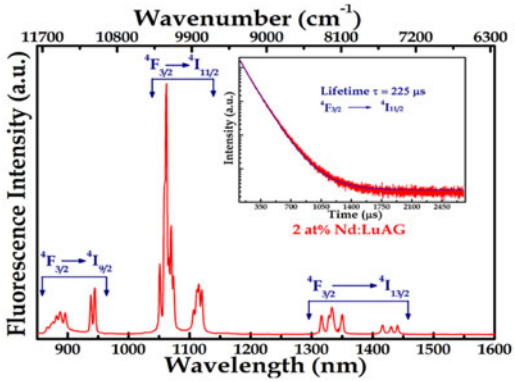

Fig. 5. Fluorescence spectrum of 2 at% Nd:LuAG transparent ceramic. (Inset) Decay curve for 1064 nm emission.

TABLE 2
Estimated Fluorescence Line Strengths (S_{calc}), Radiative Transition Rates ($A_{JJ'}$), Branching Ratios ($B_{JJ'}$), and Radiative Lifetime (τ_r) of Nd^{3+} Ions Doped LuAG Ceramic at 300 K

Transition (from $^4F_{3/2}$)	$[U^{(2)}]^2$	$[U^{(4)}]^2$	$[U^{(6)}]^2$	$\bar{\lambda}$ (nm)	$n(\bar{\lambda})$	S_{calc} (10^{-21} cm^2)	$A_{JJ'}$ (s-1)	$B_{JJ'}$ (%)	τ_r (μs)
$^4I_{9/2}$	0	0.2293	0.0548	910	1.7736	0.6575	1032	28.9	
$^4I_{11/2}$	0	0.1136	0.4104	1073	1.7714	2.1675	2067	57.8	
$^4I_{13/2}$	0	0	0.2085	1353	1.7695	1.002	475	13.3	280

reduced matrix elements for these transitions are taken from literature [30]. The radiative transition probabilities $A(J \rightarrow J')$ is calculated for the transitions by using the following expression:

$$A\left(J \rightarrow J'\right) = \frac{64\pi^4 e^2}{3h\varepsilon_0 \bar{\lambda}^3 (2J+1)} \frac{n(\lambda)\left(n(\lambda)^2+2\right)^2}{9} S_{calc}\left(J \rightarrow J'\right). \tag{10}$$

The radiative lifetime τ_r of the excited state ^4F_J $(J = 3/2)$ is calculated by taking the reciprocal of the sum of transition probabilities

$$\tau_r = \frac{1}{\sum_{J'} A\left(J \rightarrow J'\right)} \tag{11}$$

and the fluorescence branching ratios $\beta(J \rightarrow J')$ for transition originating on an initial ^4F_J $(J = 3/2)$ manifold to one possible terminal manifolds $^4I_{J'}(J' = 13/2, 11/2, 9/2)$ is determined from radiative transition rates by using the following equation:

$$\beta\left(J \rightarrow J'\right) = \frac{A\left(J \rightarrow J'\right)}{\sum_{J'} A\left(J \rightarrow J'\right)} = A\left(J \rightarrow J'\right)\tau_r. \tag{12}$$

The calculated values of emission line strengths, radiative transition rates, and fluorescence branching ratios for $^4F_{3/2} \rightarrow {}^4I_{9/2}$, $^4I_{11/2}$, and $^4I_{13/2}$ are listed in Table 2. The radiative lifetime for transitions ^4F_J $(J = 3/2) \rightarrow {}^4I_{J'}(J' = 13/2,\ 11/2,\ 9/2)$ was determined to be 280 μs, and the room temperature fluorescence lifetime of $^4F_{3/2} \rightarrow {}^4I_{11/2}$ is measured to be 225 μs. Therefore, the

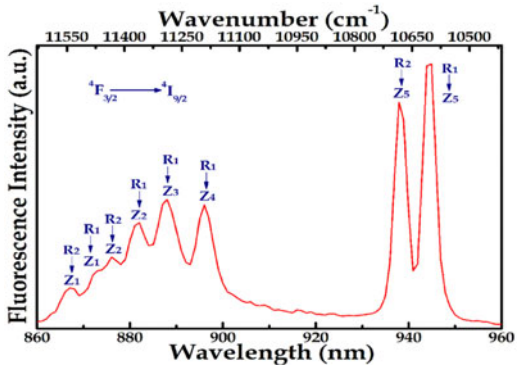

Fig. 6. Fluorescence spectrum of Nd^{3+} in transparent ceramic LuAG for the manifold $^4F_{3/2} \rightarrow {}^4I_{9/2}$ transition at room temperature.

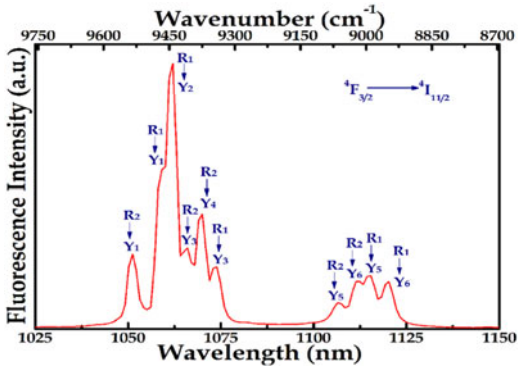

Fig. 7. Fluorescence spectrum of Nd^{3+}:LuAG ceramic for the manifold $^4F_{3/2} \rightarrow {}^4I_{11/2}$ transition at room temperature.

fluorescence quantum efficiency of the $^4F_{3/2} \rightarrow {}^4I_{11/2}$ transition, calculated from the measured room temperature fluorescence lifetime and the radiative lifetime [31], is evaluated to be 80.4%.

3.3 Inter-Stark and Inter-Manifold Emission Cross Sections

The inter-Stark emission cross sections can be determined from the corresponding spectral line shapes, which are well fitted by a Gaussian distribution with a respective full width at half maximum (FWHM). A Gaussian line shape is indicative of inhomogeneous broadening coming from changes in the local Nd^{3+} sites symmetry, as a result of the substitution from Nd^{3+} ions on the Y^{3+} ions sites. The peak emission cross section for the inter-Stark transition is one of the most important parameters of laser design because it describes the maximum spatial amplification of emission intensity. The detailed characterization of the Stark energy levels of $^4I_{9/2}$, $^4I_{11/2}$, and $^4I_{13/2}$ multiplets have been determined from the room temperature emission spectra within the manifold $^4F_{3/2} \rightarrow {}^4I_{9/2}$, $^4I_{11/2}$, and $^4I_{13/2}$ transitions of Nd^{3+} in LuAG ceramic, as shown in Figs. 6–8, respectively.

The peak emission cross sections for all Stark transitions can be expressed by the following equations [32]–[34]:

$$\sigma_p\left(R_{1,2} \rightarrow X, Y, Z\right) = \frac{{\lambda_p}^2}{4\pi c n^2 \Delta\bar{\nu}} \left[\frac{\ln 2}{\pi}\right]^{1/2} A\left(R_{1,2} \rightarrow X, Y, Z\right) \tag{13}$$

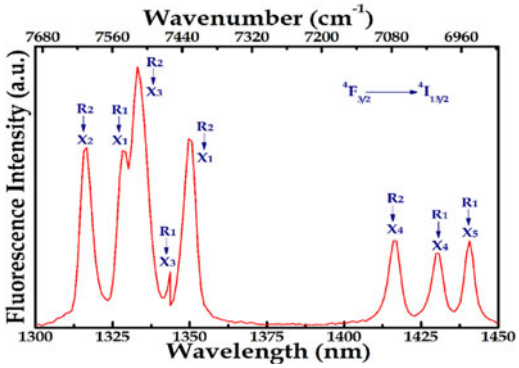

Fig. 8. Fluorescence spectrum of Nd^{3+} in transparent ceramic LuAG for the manifold $^4F_{3/2} \rightarrow {}^4I_{13/2}$ transition at room temperature.

where λ_p is the wavelength at the peak position of the emission band, $\Delta\bar{\nu}$ denotes the FWHM line width, n is the refractive index at λ_p, and c is the speed of light. The radiative probabilities of the inter-Stark transitions $R_{1,2} \rightarrow X, Y, Z$ can be expressed in the following respective equations:

$$A\left(R_{1,2} \rightarrow X_i\right) = \left(1 + e^{-\Delta/kT}\right) \beta\left(R_{1,2} \rightarrow X_i\right) \beta\left({}^4F_{3/2} \rightarrow {}^4I_{13/2}\right) \tau_r\left({}^4F_{3/2}\right)^{-1} \quad (14)$$

$$A\left(R_{1,2} \rightarrow Y_j\right) = \left(1 + e^{-\Delta/kT}\right) \beta\left(R_{1,2} \rightarrow Y_j\right) \beta\left({}^4F_{3/2} \rightarrow {}^4I_{11/2}\right) \tau_r\left({}^4F_{3/2}\right)^{-1} \quad (15)$$

$$A\left(R_{1,2} \rightarrow Z_k\right) = \left(1 + e^{-\Delta/kT}\right) \beta\left(R_{1,2} \rightarrow Z_k\right) \beta\left({}^4F_{3/2} \rightarrow {}^4I_{9/2}\right) \tau_r\left({}^4F_{3/2}\right)^{-1} \quad (16)$$

where Δ is the difference in energy between the Stark levels R_1 and R_2 of the $^4F_{3/2}$ manifold and herein is about 79 cm^{-1}. k is the Boltzman constant, T is the absolute temperature, $\tau_r(4F_{3/2})$ is the radiative lifetime of the $^4F_{3/2}$ level. $\beta({}^4F_{3/2} \rightarrow {}^4I_{13/2})$, $\beta({}^4F_{3/2} \rightarrow {}^4I_{11/2})$, and $\beta({}^4F_{3/2} \rightarrow {}^4I_{9/2})$ are the branching ratios for the respective intermanifold transitions. $\beta(R_{1,2} \rightarrow X_i)$, $\beta(R_{1,2} \rightarrow Y_j)$, and $\beta(R_{1,2} \rightarrow Z_k)$ are the branching ratios for the inter-Stark transitions determined by dividing the area of a certain sharp inter-Stark transition band to the corresponding total area of the intermanifold transition. The peak emission cross sections of the inter-Stark transitions obtained for $^4F_{3/2} \rightarrow {}^4I_{9/2}$, $^4I_{11/2}$, and $^4I_{13/2}$ transitions are presented in Table 3. By simply adding emission cross-section of each Stark levels, the total emission cross-section for $^4F_{3/2} \rightarrow {}^4I_{9/2}$, $^4I_{11/2}$, and $^4I_{13/2}$ transitions is calculated to be 7.41×10^{-20} cm^2, 29.83×10^{-20} cm^2, and 10.53×10^{-20} cm^2, respectively.

3.4 CW Laser Performances

In laser experiment, a V-shaped resonator cavity was adopted to evaluate laser performances of Nd:LuAG transparent ceramic, as shown in Fig. 9. The ceramic specimen was pumped by a LD emitting at 808 nm (maximum power: 30 W) at the end of the fiber (core diameter: 200 μm; numerical aperture: 0.22). The pump laser beam was focused into the Nd^{3+}-doped LuAG ceramic through an optical focusing and collimating system (OFCS) composed of two doublet lenses with a focal length of 49.8 mm and a nominal magnification of 1:0.8. The resonator consisted of three mirrors. The flat mirror (M1) has an anti-reflection coating at 808 nm and high reflectivity at 1064 nm. The folding mirror (M2) with a curvature radius of 200 mm has high reflectivity at 1064 nm. The output coupler (OC) was partially reflection coated at 1064 nm with a series of transmission (T_{OC} = 0.8, 2.0, 5.0, 10.0, and 15.0%). The ceramic specimen with dimensions of $5.1 \times 7.9 \times 2.1$ mm^3 was antireflection coated (HT: 808 and 1064 nm) at both large faces, and was wrapped with indium foil on a copper heat sink maintaining at 14 °C and, finally, was placed near M1.

TABLE 3

Radiative Properties of Various Stark Levels Observed for the Transitions Within the Manifold $^4F_{3/2} \rightarrow {}^4I_{9/2}$, $^4I_{11/2}$, and $^4I_{13/2}$

Transition (from $^4F_{3/2}$ to)	Inter-Stark transitions	λ_p (nm)	n	$\beta(R \rightarrow X, Y, Z)$	$A(R \rightarrow X, Y, Z)$ (s^{-1})	$\Delta\bar{\nu}$ (cm^{-1})	$\sigma_p(R \rightarrow X, Y, Z)$ (10^{-20} cm^2)
$^4I_{9/2}$	$R_2 \rightarrow Z_1$	867	1.7744	0.0410	3.5514	63.84	0.1593
	$R_1 \rightarrow Z_1$	873	1.7743	0.0345	2.9884	47.30	0.1835
	$R_2 \rightarrow Z_2$	876	1.7742	0.0636	5.5091	50.12	0.3214
	$R_1 \rightarrow Z_2$	882	1.7741	0.1026	8.8873	38.69	0.6811
	$R_1 \rightarrow Z_3$	888	1.7740	0.1742	15.0894	73.57	0.6167
	$R_1 \rightarrow Z_4$	896	1.7738	0.1215	10.5244	12.45	2.5877
	$R_2 \rightarrow Z_5$	938	1.7732	0.2082	18.0345	68.19	0.8877
	$R_1 \rightarrow Z_5$	944	1.7731	0.2544	22.0364	38.11	1.9685
$^4I_{11/2}$	$R_2 \rightarrow Y_1$	1051	1.7717	0.0888	15.3839	30.76	2.1128
	$R_1 \rightarrow Y_1$	1058	1.7716	0.1379	23.8901	22.31	4.5872
	$R_1 \rightarrow Y_2$	1062	1.7716	0.3005	52.0593	26.61	8.4347
	$R_2 \rightarrow Y_3$	1066	1.7715	0.0745	12.9065	22.88	2.4502
	$R_2 \rightarrow Y_4$	1070	1.7715	0.1228	21.2742	24.47	3.8033
	$R_1 \rightarrow Y_3$	1073	1.7714	0.0719	12.4561	22.31	2.4610
	$R_2 \rightarrow Y_5$	1107	1.7712	0.0330	5.7169	34.29	0.7811
	$R_2 \rightarrow Y_6$	1112	1.7711	0.0490	8.4889	25.89	1.5499
	$R_1 \rightarrow Y_5$	1115	1.7711	0.0596	10.3252	25.73	1.9089
	$R_1 \rightarrow Y_6$	1120	1.7710	0.0620	10.7410	29.49	1.7480
$^4I_{13/2}$	$R_2 \rightarrow X_2$	1316	1.7697	0.1731	6.9004	28.84	1.5889
	$R_1 \rightarrow X_1$	1327	1.7696	0.0824	3.2848	19.29	1.1496
	$R_2 \rightarrow X_3$	1333	1.7696	0.3461	13.7968	37.38	2.5139
	$R_1 \rightarrow X_3$	1343	1.7695	0.0208	0.8292	12.19	0.4704
	$R_2 \rightarrow X_1$	1350	1.7695	0.1491	5.9436	22.49	1.8465
	$R_2 \rightarrow X_4$	1416	1.7692	0.0843	3.3605	25.92	0.9970
	$R_1 \rightarrow X_4$	1430	1.7692	0.0726	2.8941	25.42	0.8928
	$R_1 \rightarrow X_5$	1440	1.7691	0.0713	2.8422	21.20	1.0668

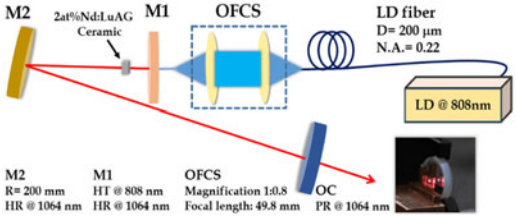

Fig. 9. Schematic diagram of laser-diode pumped CW laser based on an Nd^{3+}-doped LuAG transparent ceramic.

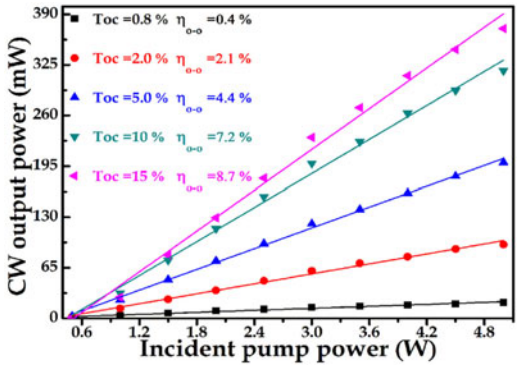

Fig. 10. CW laser output power versus the incident pump power for the fabricated 2 at% Nd:LuAG transparent ceramic. T_{OC}, output coupler transmission; η_{O-O}, optical-to-optical conversion efficiency.

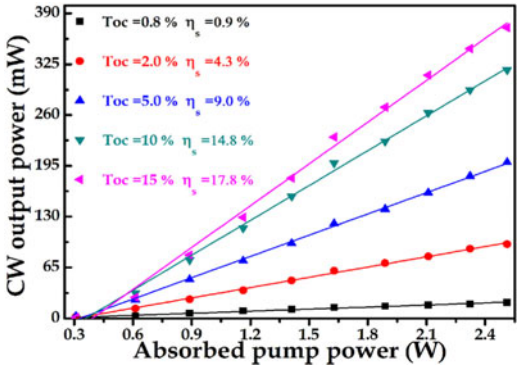

Fig. 11. CW laser output power versus the absorbed pump power for the fabricated 2 at% Nd:LuAG transparent ceramic. T_{OC}, output coupler transmission; η_s, slop efficiency.

The relationship between the CW output power and the incident pump power obtained under several OCs ($T_{OC} = 0.8$, 2.0, 5.0, 10.0, and 15.0%) was exhibited in Fig. 10. It can be seen that the CW output power increases with the rise of incident pump power as well as the transmittance of the OCs, and that no CW output power saturation occurs at the highest incident pump power, indicating that further power scaling should be possible. Under an OC with 15% transmittance, the optical-to-optical efficiency within the whole operation range was evaluated to be 8.7% with a threshold at an incident pump power of 0.5 W.

Fig. 11 reports the CW laser output power as a function of the absorbed pump power obtained by using several OCs with different transmission. The slop efficiency was determined by a linear regression and increased with the rise of transmittance of the OCs. The highest output power (371 mW) with an absorbed pump power threshold of 0.35 W and maximum slop efficiency (17.8%) were realized with $T_{OC} = 15\%$, and further power scaling is possible with higher pumping power. The emission wavelength was measured to be 1064nm for all OCs, as shown in Fig. 12. We estimated the cavity loss using the obtained slop efficiencies under certain OCs. The round-trip cavity loss L is given by [2]

$$L = \frac{(T_2/T_1)\,T_1 - (\eta_2/\eta_1)\,T_2}{\eta_2/\eta_1 - T_2/T_1} \tag{17}$$

where η_1 and η_2 are the slop efficiencies when the OCs with transmittance of T_1 and T_2 are used, respectively. Herein, for $T_1 = 10\%$ and $T_2 = 15\%$, the cavity loss of the laser system was calculated to be 10%.

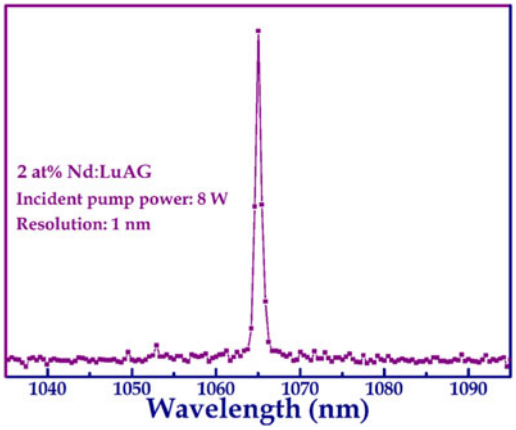

Fig. 12. Laser spectrum centered at about 1064 nm of 2 at% Nd:LuAG ceramic laser.

TABLE 4
Comparison of Spectroscopic Properties of Nd^{3+} ($4f^3$) Doped into Different Hosts

Parameters		Nd:LuAG (ceramic)[a]	Nd:Y_2O_3 (ceramic)[b]	Nd:YAG (ceramic)[c]	Nd:YAG (ceramic)[d]	Nd:YAG (crystal)[e]
Spectroscopic quality factor	$X = \Omega_4/\Omega_6$	0.32	0.96	0.69	0.67	0.54
Branching ratios	$\beta(^4F_{3/2} \rightarrow {}^4I_{9/2})$	0.29	0.43	0.38	0.41	0.37
	$\beta(^4F_{3/2} \rightarrow {}^4I_{11/2})$	0.58	0.47	0.51	0.48	0.50
	$\beta(^4F_{3/2} \rightarrow {}^4I_{13/2}))$	0.13	0.10	0.11	0.11	0.13
Radiative lifetime	$\tau_r(^4F_{3/2})$ (μs)	280	1700	316	238	250
Quantum efficiency	η (%)	80.4	61.18	77.5	88.8	88.5

Reported in this work, [b]Data from [35], [c]Data from [33], [d]Data from [36], [e]Data from [37].

4. Conclusion

In summary, the 2 at% Nd:LuAG transparent ceramic was fabricated by using tape-casting method and solid-state reactive sintering technology. The EDS spectra indicated that the atoms proportion was 1.95 at% $Nd:Lu_3Al_{4.8}O_{11.9}$ and was in close proximity to the theoretical ratio with some experimental uncertainties. The Judd-Ofelt analysis was applied to the room temperature absorption spectrum and the J-O intensity parameters were determined to be $\Omega_2 = 0.63 \times 10^{-21}$ cm^2, $\Omega_4 = 1.55 \times 10^{-21}$ cm^2, and $\Omega_6 = 4.78 \times 10^{-21}$ cm^2. Then, the absorption line strength and the radiative transition probabilities were presented. The branching ratios for $^4F_{3/2} \rightarrow {}^4I_{9/2}$, $^4I_{11/2}$, and $^4I_{13/2}$ transitions were 0.29, 0.58, and 0.13, respectively. The little spectroscopic quality factor, $X = \Omega_4/\Omega_6 = 0.32$, meaning that the efficiency of the $^4F_{3/2} \rightarrow {}^4I_{11/2}$ transition was enhanced with Nd^{3+} ions doped in the LuAG host, as shown in Table 4, which displayed the compared spectroscopic properties of Nd^{3+} ions doped in LuAG ceramic, Y_2O_3 ceramic, YAG ceramic, and YAG crystal host. The fluorescence quantum efficiency of the $^4F_{3/2} \rightarrow {}^4I_{11/2}$ transition was evaluated to be 80.4%, which was determined from the measured room temperature fluorescence lifetime (225 μs) and the radiative lifetime (280 μs) and was comparable with that of Nd^{3+} ions doped YAG either in ceramic or crystal form. Besides, the inter-Stark energy levels of the $^4I_{J'}$ manifolds were performed, and the

peak emission cross sections of the ${}^4F_{3/2} \rightarrow {}^4I_{9/2}$, ${}^4I_{11/2}$, and ${}^4I_{13/2}$ and intermanifold transitions were determined. The total emission cross-section for ${}^4F_{3/2} \rightarrow {}^4I_{9/2}$, ${}^4I_{11/2}$, and ${}^4I_{13/2}$ transitions was calculated to be 7.41×10^{-20} cm^2, 29.83×10^{-20} cm^2, and 10.53×10^{-20} cm^2, respectively. Finally, the CW laser performances at about 1064 nm was achieved under an 808 nm fiber-coupled semiconductor diode laser pumping. The slop efficiency under a 15% output coupler was 17.8%, and the roundtrip cavity loss was calculated to be 10%.

Acknowledgment

The authors would like thank the editors and the anonymous reviewers for their valuable suggestions.

References

[1] A. Ikesue and T. Kinoshita, "Fabrication and optical properties of high-performance polycrystalline Nd:YAG ceramic for solid-state lasers," *J. Amer. Ceram. Soc.*, vol. 78, no. 4, pp. 1033–1040, 1995.
[2] I. Shoji, S. Kurimura, Y. Sato, and T. Taira, "Optical properties and laser characteristics of highly Nd3+-doped Y3Al5O12 ceramics," *Appl. Phys. Lett.*, vol. 77, no. 7, pp. 939–941, 2000.
[3] W. Guo *et al.*, "Fabrication and laser behaviors of Nd:YAG ceramic microchips," *J. Eur. Ceram. Soc.*, vol. 31, no. 13, pp. 2241–2246, 2011.
[4] Y. Fu *et al.*, "Fabrication and thermal effects of highly transparent polycrystalline Nd:YAG ceramics," *Opt. Mater.*, vol. 49, pp. 105–109, 2015.
[5] H. Lin *et al.*, "Diode-pumped tape casting planar waveguide YAG/Nd:YAG/YAG ceramic laser," *Opt. Exp.*, vol. 23, no. 6, pp. 8104–8112, 2015.
[6] Y. Kuwano, K. Suda, N. Ishizawa, and T. Yamada, "Crystal growth and properties of (Lu,Y)3Al5O12," *J. Cryst. Growth*, vol. 260, pp. 159–165, 2004.
[7] X. Xu *et al.*, "Crystal growth, spectral and laser properties of Nd:LuAG single crystal," *Laser Phys. Lett.*, vol. 6, no. 9, pp. 678–681, 2009.
[8] Q. Liu, M. Gong, T. Liu, Z. Sui, and X. Fu, "Efficient sub-joule energy extraction from a diode-pumped Nd:LuAG amplifier seeded by a Nd:YAG laser," *Opt. Lett.*, vol. 41, no. 22, pp. 5322–5325, 2016.
[9] A. A. Kaminskii, G. A. Bogomolova, K. S. Bagdasarov, and A. G. Petrosyan, "Luminescence, absorption and induced emission of Lu3Al5O12-Nd3+ crystals," *Opt. Spectrosc.*, vol. 39, no. 6, pp. 643–646, 1975.
[10] K. Beil, S. T. F-Thornton, F. Tellkamp, C. Kränkel, K. Petermann, and G. Huber, "Thermal and laser properties of Yb:LuAG for kW thin disk lasers," *Opt. Exp.*, vol. 18, no. 20, pp. 20712–20711, 2010.
[11] N. Wagner, B. Herden, T. Dierkes, J. Plewa, and T. Justel, "Towards the preparation of transparent LuAG:Nd3+ ceramics," *J. Eur. Ceram. Soc.*, vol. 32, no. 12, pp. 3085–3089, 2012.
[12] Y. Zhang *et al.*, "Micro-structure of grain boundary in post-annealed sinter plus HIPed Nd:Lu3Al5O12 ceramics," *Opt. Mater. Exp.*, vol. 4, no. 10, pp. 2182–2189, 2014.
[13] Y. Ye *et al.*, "Continous-wave laser operation of Nd:LuAG ceramic with ${}^4F_{3/2} \rightarrow {}^4I_{11/2}$ transition," *Opt. Mater. Exp.*, vol. 5, no. 3, pp. 611–616, 2015.
[14] P. Zhang, B. Jiang, J. Fan, X. Mao, and L. Zhang, "Effects annealing on Cr-sensitized Nd:LuAG laser ceramics," *Opt. Mater. Exp.*, vol. 5, no. 10, pp. 2209–2216, 2015.
[15] S. Qiao *et al.*, "Spectral properties and laser performance of Nd:Lu3Al5O12 ceramic," *Chin. Opt. Lett.*, vol. 13, no. 5, pp. 051602–051602, 2015.
[16] C. Xu *et al.*, "Diode-pumped Nd:LuAG ceramic laser on 4F3/2-4F13/2 transition," *Opt. Mater.*, 2016. [Online]. Available: http://dx.doi.org/10.1016/j.optmat.2016.04.021
[17] Y. Fu *et al.*, "Fabrication, microstructure and laser performance of Nd3+-doped Lu3Al5O12 transparent ceramics," *J. Eur. Ceram. Soc.*, vol. 36, pp. 655–661, 2016.
[18] Y. Fu *et al.*, "Fabrication and properties of highly transparent Yb:LuAG ceramics," vol. 664, pp. 595–601, 2016.
[19] C. Li *et al.*, "Polycrystalline Ho:LuAG laser ceramics: Fabrication, microstructure, and optical characterization," *J. Amer. Ceram. Soc.*, pp. 1–7, 2017, doi: 10.1111/jace.14771.
[20] C. Ma *et al.*, "Cation diffusion at the interface of composite YAG/Re:LuAG (Re = Nd or Yb) transparent ceramics," *J. Eur. Ceram. Soc.*, vol. 36, pp. 2555–2564, 2016.
[21] C. Ma *et al.*, "Longitudinally diode-pumped planar waveguide YAG/Yb:LuAG/YAG ceramic laser at 1030.7 nm," *Opt. Lett.*, vol. 41, no. 14, pp. 3317–3319, 2016.
[22] C. Ma *et al.*, "Spectral and laser properties of Yb:LuAG transparent ceramics fabricated by tape casting method," *J. Amer. Ceram. Soc.*, vol. 99, no. 10, pp. 3267–3272, 2016.
[23] B. R. Judd, "Optical absorption intensities of rare-earth ions," *Phys. Rev.*, vol. 127, no. 3, pp. 750–761, 1962.
[24] G. S. Ofelt, "Intensities of crystal spectra of rare-earth ions," *J. Chem. Phys.*, vol. 37, no. 3, pp. 511–520, 1962.
[25] G. Singh, V. S. Tiwari, and P. K. Gupta, "Spectroscopic analysis on the basis Judd-Ofelt theory of Nd3+ in (Y0.985Nd0.015)2O3: A transparent laser-host ceramic," *Mater. Res. Bull.*, vol. 60, pp. 838–842, 2014.
[26] M. J. Weber, "Radiative and multiphonon relaxation of rare-earth ions in Y2O3," *Phys. Rev.*, vol. 171, no. 2, pp. 283–291, 1968.
[27] M. J. Weber and T. E. Varitimos, "Optical spectra and intensities of Nd3+ in YAlO3," *J. Appl. Phys.*, vol. 42, no. 12, pp. 4996–5005, 1971.

[28] R. C. Powell, *Physics of Solid State Laser Materials*. New York, NY, USA: Springer, 1998.
[29] A. A. Kaminskii, *Laser Crystals*, vol. 14. New York, NY, USA: Springer-Verlag, 1981, pp. 164–165.
[30] A. A. Kaminskii, *Crystalline Lasers: Physical Process and Operating Schemes* (Laser and Optical Science and Technology Series). New York, NY, USA: CRC, 1996.
[31] G. D. Yoder, P. K. Diwakar, and D. W. Hahn, "Assessment of soot particle vaporization effects during laser-induced incandescence with time-resolved light scattering," *Appl. Opt.*, vol. 44, no. 20, pp. 4211–4219, 2005.
[32] M. Pokhrel, N. Ray, G. A. Kumar, and D. K. Sardar, "Comparative studies of the spectroscopic properties of Nd3+:YAG nanocrystals, transparent ceramic and single crystal," *Opt. Mater. Exp.*, vol. 2, no. 3, pp. 235–249, 2012.
[33] D. K. Sardar, R. M. Yow, J. B. Gruber, T. H. Allik, and B. Zandi, "Stark components of lower-lying manifolds and emission cross-sections of intermanifold and inter-Stark transitions of Nd3+ (4f3) in polycrystalline ceramic garnet Y3Al5O12," *J. Lumin.*, vol. 116, no. 1/2, pp. 145–150, 2006.
[34] W. F. Krupke, M. D. Shinn, J. E. Marion, J. A. Caird, and S. E. Stokowski, "Spectroscopic, optical, and thermomechanical properties of neodymium- and chromium-doped gadolinium scandium gallium garnet," *J. Opt. Soc. Amer. B*, vol. 3, no. 1, pp. 102–114, 1986.
[35] D. K. Sardar, D. M. Dee, K. L. Nesh, R. M. Yow, and J. B. Gruber, "Optical absorption intensity analysis and emission cross sections for the intermanifold and the inter-Stark transitions of Nd3+(4f3) in polycrystalline ceramic Y2O3," *J. Appl. Phys.*, vol. 100, 2006, Art. No. 123106.
[36] G. A. Kumar *et al.*, "Spectroscopic and stimulated emission characteristics of Nd3+ in transparent YAG ceramics," *IEEE J. Quantum Electron.*, vol. 40, no. 6, pp. 747–758, Jun. 2004.
[37] W. F. Krupke, "Radiative transition probabilities within the 4f3 ground configuration of Nd:YAG," *IEEE J. Quantum Electron.*, vol. QE-7, no. 4, pp. 153–159, Apr. 1971.